Linking hydrophobicity and hydrodynamics by the hybrid fluctuating hydrodynamics and molecular dynamics methodologies

Nikolaos K. Voulgarakis
Department of Chemical and Biomolecular Engineering, University of California, Berkeley, Berkeley, California 94720, USA and Department of Mathematics, Washington State University, Richland, Washington 99372, USA

Barry Z. Shang
Department of Chemical and Biomolecular Engineering, University of California, Berkeley, Berkeley, California 94720, USA

Jhih-Wei Chu*
Department of Chemical and Biomolecular Engineering, University of California, Berkeley, Berkeley, California 94720, USA; Department of Biological Science and Technology, National Chiao Tung University, Hsinchu, Taiwan, Republic of China; and Institute of Bioinformatics and Systems Biology, National Chiao Tung University, Hsinchu, Taiwan, Republic of China
(Received 16 March 2013; revised manuscript received 11 June 2013; published 27 August 2013)

The development of a hybrid fluctuating hydrodynamics (FHD) and molecular dynamics (MD) simulation method that combines the molecular dynamics of moving particles with the fluctuating hydrodynamics of solvent fields on Eulerian grid cells is presented. This method allows resolution of solute-solvent interfaces and realization of excluded volumes of particles in the presence of hydrodynamic coupling. With these capabilities, we show that the ubiquitous forces mediated by the solvent, hydrophobicity and hydrodynamics, can be linked in a mesoscopic simulation. The strategies we devise to overcome the numerical issues of mixing variables in the Eulerian and Lagrangian coordinate systems, i.e., using a pair of auxiliary fluids to realize the excluded volumes of particles and assigning collocating gridding systems on solutes to interface with solvent fields, are also presented. Simulation results show that the hybrid FHD and MD method can reproduce the solvation free energies and scaling laws of particles dynamics for hydrophobes of different sizes. The collapse of two hydrophobic particles was also simulated to illustrate that the hybrid FHD and MD method has the potential to be generally applied to study nanoscale self-assembly and dynamics-structure-function relationships of biomolecules.

DOI: 10.1103/PhysRevE.88.023305 PACS number(s): 02.70.Ns, 47.10.ad, 36.20.Ey, 47.11.−j

I. INTRODUCTION

Solvent-mediated interactions have profound influence on nanoscale self-assembly and the dynamics-structure-function relationships of biomolecules [1]. The atomic construct and electronic structure of the water molecule render its room-temperature liquid state to have a unique hydrogen bonding network, strong cohesive energy, and high surface tension [2]. Solvent-solute interactions, local perturbation in the hydrogen bonding network, and formation of liquid-vapor- or liquid-liquid-like interfaces together can cause multiscale and multifaceted responses in the aqueous solvation of foreign molecules [3,4]. The free-energy landscapes of biomolecule conformation and nanoparticle arrangement are thus a strong function of water-mediated forces [5,6].

Another important class of solvent effects is hydrodynamics governed by the constraints of conservation laws. Liquid water has high viscosity and low isothermal compressibility at room temperature to give rise to the specific properties of dynamic relaxation and energy dissipation in the condensed phase [7–9]. Furthermore, at the nanoscale such as close to phase boundaries, thermal fluctuations have significant magnitudes and cannot be neglected [10]. Design and engineering of nanostructures and functions thus face the complexities of solvation effects coupled with hydrodynamic forces under the influence of stochastic noises. In this regard, computer simulation can potentially be used to integrate physical models across different spatial and temporal scales to elucidate how the behaviors of a molecular system emerge through the convolution of various forces.

Molecular dynamics (MD) simulations provide a way to incorporate atomistic details of the solvent, but suffer from requiring a small time step of integration and spending the majority of computational resource on evaluating the less interesting solvent-solvent interactions. Although specially designed hardware and software may overcome these issues to some extent [11], the accessible time and length scales of all-atom MD are still severely limited. If mesoscopic models could be developed to capture the essential physics mediated by the solvent, with hydrophobicity and hydrodynamics as the two critical components, computer simulation can be conducted at more realistic length scales and reach longer time scales. In this work, we aim to fulfill this objective using the fluctuating hydrodynamics (FHD) of Landau and Lifshitz to capture the hydrodynamics of solvent fluctuations at the nanoscale.

Recently, it was shown that the FHD equations can be employed to transform the results of all-atom MD simulations onto mesoscopic fluid dynamics with quantitative self-consistency [12–16]. Density distributions, flow profiles, and their fluctuations in an atomic-scale simulation can be mapped onto the field variables in FHD equations. This mapping allows extraction of the required equations of state, response

*Corresponding author: jwchu@nctu.edu.tw

functions, and transport coefficients from the recorded positions and velocities of atoms for reproducing the observed profiles and statistics in simulations using the FHD model. With this compatibility in describing hydrodynamics, FHD is adopted in this work to couple with the particulate degrees of freedom in a hybrid model to capture hydrophobicity.

Schemes for coupling a mesoscopic solvent with the MD of particles have been intensively developed with the goal of effective simulation of nanoscale systems. A number of mesoscopic solvent models including FHD were thus proposed [17–28]. However, developments in this regard focused on either capturing hydrophobicity or describing hydrodynamics. This work presents the development of a hybrid FHD and MD simulation methodology that resolves the boundaries between fluctuating solvent fields and solute particles. The hybrid FHD and MD model thus allows an explicit representation of solvation effects by realizing cavity formation while retaining the effects of interfacial fluctuations and hydrodynamic couplings.

The rest of this paper is organized as follows. We first present the components of the ansatz we devised for hybridizing the mechanics of FHD and MD. The local free-energy densities of the solvent fluid and solute-solvent interactions, representation of particles in the solvent fluid, and the auxiliary fluids and their dynamics for realizing the excluded volumes of particles are discussed in detail. The success of using the hybrid FHD and MD methodology in capturing important phenomena induced by hydrophobicity and hydrodynamics is then presented. We also compare the results of hybrid FHD and MD simulations with those obtained by all-atom MD simulations. Specifically, the size dependence of solvation free energies of hydrophobes, the potentials of mean forces of associating two hydrophobic particles, the scaling laws of velocity autocorrelation functions of particle dynamics, and the feature of Stokes-Einstein diffusion are computed to illustrate the feasibility of linking hydrophobicity and hydrodynamics in a hybrid model of field and particulate variables. Finally, a summary is presented.

II. HYBRIDIZATION OF CONTINUUM AND MOLECULAR MECHANICS UNDER THERMAL FLUCTUATIONS

The goal of stitching together continuum and molecular mechanics in the hybrid FHD and MD methodology is to capture the equilibrium as well as nonequilibrium behaviors of nanoscale systems. In particular, the following objectives are desired. First, the hybrid model should be able to represent the solvation free energy for accommodating finite-size molecules in the solution. Second, the motions of particles must have proper hydrodynamic responses. Third, the fluctuations of both the field and particulate degrees of freedom need to satisfy the requirements of thermal equilibrium.

To accomplish the aforementioned requirements, we developed an ansatz of hybrid mechanics to combine FHD and MD for representing the excluded volumes of moving objects and the solvent-particle interactions. The length scale of grid cells for discretizing the space of a simulation model in our scheme (see Fig. 1) is chosen to be 5 Å. At this level of spatial resolution, continuum mechanics is still applicable for describing liquid-state water at room temperature [12–16]. Coupling the Eulerian gridding of FHD variables with nanoparticles whose sizes are at a similar length scale, however, can cause unphysical phenomena such as spurious currents of fluids [29], negative densities [15], and the tendency of particles to stick in specific locations [30]. The design of our hybridization scheme for which the components are presented in the following is to avoid these problems while achieving the objectives stated in the preceding paragraph.

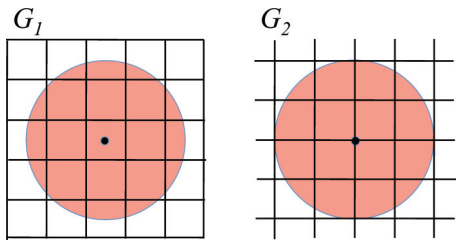

FIG. 1. (Color online) A solute particle and the two Lagrangian girding systems imposed in the hybrid FHD and MD methodology. Each grid cell has a specific volume that is occupied by the particle for which the symbol is $V_{\rm occ}$. Depending on the relative position of the particle, the values of $V_{\rm occ}$ for grid cells vary from zero to $V_{\rm c}$, the cell volume. For grid cells inside the particle, its $V_{\rm occ}$ is equal to $V_{\rm c}$ since the entire grid cell is occupied by the particle.

A. Local free-energy densities of the fluid and the solvent-particle interactions

Surrounding particles such as the one shown in Fig. 1 is the solvent fluid with a local free-energy density of $F_0[\rho(\mathbf{x})]$; $\rho(\mathbf{x})$ is the fluid density at the Eulerian grid cell of position $\mathbf{x}$. To build in the capability of describing the phenomenon of solvation, we model F_0 with an intrinsic free-energy density of a homogeneous fluid that allows vapor-liquid coexistence. Without loss of generality, a simple symmetrical double-well potential with minima at the vapor density $\rho_{\rm v}$ and liquid density $\rho_{\rm l}$ is employed:

$$\psi[\rho(\mathbf{x})] = \frac{C}{2}[\rho(\mathbf{x}) - \rho_{\rm l}]^2[\rho(\mathbf{x}) - \rho_{\rm v}]^2. \tag{1}$$

Furthermore, we also incorporate the square gradient of density fields and a surface tension coefficient m in F_0. Therefore,

$$F_0[\rho(\mathbf{x})] = \int \left[\psi[\rho(\mathbf{x})] + \frac{m}{2}|\nabla\rho(\mathbf{x})|^2\right] d^3x. \tag{2}$$

To represent the excluded volumes of particles and resolve solute-solvent interfaces in the solvent environment, $F_{\rm ps}$, the local free-energy density due to solvent-particle interactions, is imposed. Motivated by the Gaussian fluctuations of density fields observed over a wide range of thermodynamic states [31], we employ a quadratic form for representing $F_{\rm ps}$:

$$F_{\rm ps}[\rho(\mathbf{x})] = \int \frac{k}{2}\left(\frac{V_{\rm occ}(\mathbf{x})}{V_{\rm c}}\right)^2 \rho(\mathbf{x})^2 d^3x. \tag{3}$$

Here k is the strength of energy penalty for excluding particle volumes in a hybrid FHD and MD simulation. For the fluid grid cell at $\mathbf{x}$, $V_{\rm occ}(\mathbf{x})$ is the part of the cell volume that is occupied by the particle (see Fig. 1). In this work, all Eulerian grid cells for the solvent fluid have the same volume of $V_{\rm c} = 125\ \text{Å}^3$.

The form of F_{ps} in Eq. (3) disfavors the presence of liquid inside the particle to prevent the fluid from flowing in. Therefore, F_{ps} predominantly comes from the cells overlapping the particle surface in simulations as ρ inside the particle has very small values around ρ_v and $V_{occ}(\mathbf{x})$ is zero outside the particle. The total free-energy density at a specific location in the simulation model is thus

$$F[\rho(\mathbf{x})] = F_0[\rho(\mathbf{x})] + F_{ps}[\rho(\mathbf{x})]. \tag{4}$$

The combined effects of F_0 and F_{ps} would then create a vapor-liquid interface around a particle in the solvent. The values of C, m, and k can be determined by reproducing the solvation free energy of particles and other observables of liquid water.

B. Representation of particles in the solvent fluid

To imprint solutes onto the Eulerian grid cells of fluid fields, each particle is assigned a collocating gridding system composed of cubic cells as shown in Fig. 1. The Lagrangian grid cells associated with a particle record the different parts of the total excluded volume. If an on-particle cell is within the solute, V_{occ} is equal to the cell size. For cells covering the particle surface, the corresponding V_{occ} have smaller values. The size of the Lagrangian grid cells of particles thus dictates the intensity of numerical nodes for resolving the space occupied by the solute. A smaller cell size gives a better resolution but adds a larger number of parameters for describing each particle. A larger size, in contrast, gives a blurrier view of particles with a less expensive representation. In this work, the size of Lagrangian cubic cells moving with the particle is chosen to have the same size as the Eulerian cells of field variables for consistency in the spatial resolution of particulate and field variables.

In addition to facilitating the calculation of the volume occupied by particles in Eulerian cells, introducing Lagrangian grid cells associated with a solute also provides a convenient way to determine the profiles of solvent variables such as the density ρ and velocity $\mathbf{v}$ around the particle via interpolation. Since the overlapping between two cubic cells can be trivially calculated given their centers, quantities associated with a Lagrangian cell can be distributed to the overlapping Eulerian cells and vice versa based on their common volumes in space. For example, the values of V_{occ} of the Lagrangian cells for a solute can inform local Eulerian cells of the presence of the particle. The resulting changes in free-energy density on Eulerian cells can then be fed back to the particle grids to calculate the concomitant forces coming from the fluid.

In this way, the N Lagrangian cells of a particle locating at $\mathbf{X}$ compose a set of nonoverlapping interpolation functions with the shape of a cubic δ function and $\mathbf{X}_j$'s as their centers, $\delta_c(\mathbf{x} - \mathbf{X}_j)$, $j = 1, \ldots, N$. These functions collocating with the particle are normalized such that $\sum_{i=1}^{M}\sum_{j=1}^{N}\delta_c(\mathbf{x}_i - \mathbf{X}_j) = 1$. Here the $\mathbf{x}_i$ are the centers of M Eulerian grid cells that are used to discretize the space within the simulation box. Therefore, for any quantity B such as V_{occ} whose values on the Lagrangian cells of a particle locating at $\mathbf{X}$ are known, the corresponding value on an overlapping Eulerian cell locating at $\mathbf{x}_i$ is then

$$B(\mathbf{x}_i) = \sum_{j=1}^{N}\delta_c(\mathbf{x}_i - \mathbf{X}_j)B(\mathbf{X}_j). \tag{5}$$

Similarly, $B(\mathbf{x}_i)$ on Eulerian cells can be combined with the Lagrangian grids of this particle as

$$B(\mathbf{X}_j) = \sum_{i=1}^{M}\delta_c(\mathbf{x}_i - \mathbf{X}_j)B(\mathbf{x}_i). \tag{6}$$

The occupied volume $V_{occ}(\mathbf{X}_j)$ for each Lagrangian cell is precalculated as the part of the cell overlapping with the solute (Fig. 1). Overall, the following equation of volume conservation of the particle is satisfied:

$$\sum_{i=1}^{M}\sum_{j=1}^{N}\delta_c(\mathbf{x}_i - \mathbf{X}_j)V_{occ}(\mathbf{X}_j) = \frac{4\pi}{3}R^3. \tag{7}$$

To calculate solute-solvent interaction energies and forces via Eq. (3) the following scheme is used to calculate the densities and density gradients $\rho(\mathbf{X}_j)$ and $\nabla\rho(\mathbf{X}_j)$ on the Lagrangian grids of each particle. First, the solvent density filled in a Lagrangian cell is treated like a pseudoparticle and interacts with the solute radially. Second, estimation of density gradients on Lagrangian grids is based on the values a distance l away inward and outward radially. That is,

$$\begin{aligned}\rho(\mathbf{X}_j) &\simeq \frac{\rho(\mathbf{X}_j + l\hat{\mathbf{r}}) + \rho(\mathbf{X}_j - l\hat{\mathbf{r}})}{2},\\ \frac{\partial\rho}{\partial r}(\mathbf{X}_j) &\simeq \frac{\rho(\mathbf{X}_j + l\hat{\mathbf{r}}) - \rho(\mathbf{X}_j - l\hat{\mathbf{r}})}{2l}.\end{aligned} \tag{8}$$

This approach is to alleviate the spatially dependent bias in estimating $\rho(\mathbf{X}_j)$ and $\partial\rho(\mathbf{X}_j)/\partial r$ when projecting Lagrangian grids onto Eulerian cells with a finite resolution. Such uneven estimation is most prominent on grids covering the particle surface. Using the values with a distance l away significantly reduces this issue along the directions of density gradients. For particles with a diameter less than 10 Å, l is the particle diameter. For particles with a diameter larger than 10 Å, l is fixed at 10 Å. Furthermore, if another particle is within 10 Å of the focused particle, l is reduced to shift away from the inside of the neighboring particle.

The resulting values of $\rho(\mathbf{X}_j)$ and $\partial\rho(\mathbf{X}_j)/\partial r$ are then used to approximate the solvent-particle interactions

$$\begin{aligned}\mathbf{f}_p(\mathbf{X}_j) \approx -k\left(\frac{V_{occ}(\mathbf{X}_j)}{V_c}\right)^2\rho(\mathbf{X}_j)\frac{\partial\rho}{\partial r}\rho(\mathbf{X}_j)\hat{\mathbf{r}}\\ -\frac{\gamma_0}{\rho_l}\rho(\mathbf{X}_j)[\mathbf{V} - \mathbf{v}(\mathbf{X}_j)] + \mathbf{s}(\mathbf{X}_j),\end{aligned} \tag{9}$$

$$\mathbf{f}_f(\mathbf{x}_i) = -\sum_{j=1}^{N}\delta_c(\mathbf{x}_i - \mathbf{X}_j)\mathbf{f}^p(\mathbf{X}_j). \tag{10}$$

Here $\hat{\mathbf{r}}$ is the radial unit vector along the distance r between $\mathbf{X}_j$ and the center of the particle; $f_p(\mathbf{X}_j)$ is the force density at the particle cell of $\mathbf{X}_j$ and $f_f(\mathbf{x}_i)$ is that at the fluid cell of x_i; $\mathbf{V}$ is the velocity of the particle and $\mathbf{v}(\mathbf{X}_j)$ is the fluid velocity field estimated at $\mathbf{X}_j$.

In Eq. (9), the friction coefficient γ is treated to have a linear dependence on the fluid mass density, i.e., $\gamma = \gamma_0\rho/\rho_l$

for a continuous variation of the friction force with solvent density. The stochastic force **s** is modeled as Gaussian random noise with a covariance of

$$\langle s(\mathbf{X},t)s(\mathbf{X}',t')\rangle = 2\gamma k_{\mathrm{B}}T\delta(\mathbf{X}-\mathbf{X}')\delta(t-t'). \tag{11}$$

This fluctuation-dissipation coupling is employed here as a thermostat to balance the frictional and stochastic interaction forces between particles and fields for achieving thermal equilibrium in the dynamics simulation; k_{B} is the Boltzmann constant and T is the temperature. A similar approach has been used for coupling particles and the lattice Boltzmann solvent model [17,19]. The total force acting on the particle is then calculated by a numerical integration using the $\delta_{\mathrm{c}}(\mathbf{x}_i-\mathbf{X}_j)$ values on particle surfaces:

$$\mathbf{F}_{\mathrm{ps}}(\mathbf{X}) = V_{\mathrm{c}}\sum_{\mathbf{X}_j\in A}\mathbf{f}_{\mathrm{p}}(\mathbf{X}_j), \tag{12}$$

where A is the surface of the particle.

An inevitable issue that occurs in linking Lagrangian and Eulerian cells is that the projected structure of the particle onto space depends on its location in the occupying Eulerian cell [30] and the proposed scheme of using a Lagrangian griding system is not exempt. Even with the estimation of Eq. (9), this problem still causes an imbalance in the estimated field variables and their derivatives around the particle surface and generates spatially dependent forces to pin the particle at specific loci. Different strategies of using more complicated and longer-range smoothing functions have been suggested [32,33]. The arithmetic simplicity of our proposed scheme that uses a collocating gridding system on particles allows a simple way to significantly alleviate this problem. Introducing a combination of Lagrangian griding systems with different phase shifts such as G_1 and G_2 shown in Fig. 1 is found to reduce the bias due to finite-size discretization to an unnoticeable level. This approach only requires using the local interpolation functions defined in Eqs. (5) and (6) to resolve the particle interface with all of the gridding systems on the particle. Analysis of dynamic trajectories indicates that combining G_1 and G_2 is sufficient for eliminating the spatial dependence of particle motions and is used in all of the simulations performed in this work.

C. Auxiliary fluids and their dynamics for realizing excluded volumes

Although employing Eqs. (1)–(4) can indeed form a liquid-vapor boundary around a solute particle, two detrimental problems would occur in solving FHD equations in the presence of a particle-fluid interface at the nanoscale for the simulation results to be unphysical. The first issue is that under a finite-resolution discretization, numerical imbalance in evaluating the reversible stress tensor and large density gradients around a particle lead to the so-called spurious or parasitic currents, i.e., nonvanishing fluid flows in and out of the particle surface [29]. Even though a molecular scale grid cell size of 5 Å is employed, the resolution is not sufficient to precisely evaluate the density variation across the solvent-particle interface that has a thickness of only a few angstroms. Using ultrafine grid cells around the particle surface not only challenges the applicability of continuum mechanics but also significantly increases the computational cost and makes the hybrid model unappealing compared to conducting all-atom simulations.

The second issue is that there is no explicit constraint in the governing equations to disallow negative values of solvent densities inside the particle. In the presence of fluctuating field variables, negative densities inside the space of particles are unavoidable [15]. Both of the problems stated above are unphysical and their occurrence causes numerical instabilities and erroneous results. To make possible the representation of both hydrodynamics and hydrophobicity in the hybrid model, these two issues need to be overcome in a practically feasible manner.

The scheme we devised to avoid these problems is motivated by the phenomenological analogy of the phase boundaries in vapor-liquid coexistence and two immiscible liquids [15]. Using a fluid insoluble in water to fill in the space inside particles is thus an alternative way of representing their excluded volumes. The advantage of this approach is that the negative-density issue can be bypassed by not directly dealing the small numerical values of the vapor phase density. Furthermore, we consider the establishment of phase boundaries a fast molecular process since the surface thickness is smaller than the Eulerian grid cells employed in solving the FHD equations and the unstable region of the free-energy density of water in Eq. (1) is regularly visited. Resolving this fast dynamics is thus considered to be beyond the applicability of FHD as evidenced by the generation of unphysical spurious currents. The auxiliary dynamics of our hybridization scheme separates the dynamics of setting up phase boundaries from fluid advection and particle motions. It is also important to point out that the design of our hybrid methodology has the specific aim of modeling solvation phenomena in addition to capturing hydrodynamic responses and is hence distinct from the other approaches [17–28] of particle-fluid simulation.

In our scheme of hybridization, the mass density of the solvent is represented by the sum of the densities of two auxiliary fluids:

$$\rho(\mathbf{x}) = \rho^{\mathrm{A}}(\mathbf{x}) + \rho^{\mathrm{B}}(\mathbf{x}). \tag{13}$$

The local free-energy densities due to the mass densities of both components also contain the two terms of Eqs. (2) and (3) as that of the solvent:

$$F^{\mathrm{A}}[\rho^{\mathrm{A}}(\mathbf{x})] = F_0^{\mathrm{A}}[\rho^{\mathrm{A}}(\mathbf{x})] + F_{\mathrm{ps}}^{\mathrm{A}}[\rho^{\mathrm{A}}(\mathbf{x})], \tag{14}$$

$$F^{\mathrm{B}}[\rho^{\mathrm{B}}(\mathbf{x})] = F_0^{\mathrm{B}}[\rho^{\mathrm{B}}(\mathbf{x})] + F_{\mathrm{ps}}^{\mathrm{B}}[\rho^{\mathrm{B}}(\mathbf{x})]. \tag{15}$$

In Eqs. (14) and (15), the terms corresponding to homogeneous fluids for both components are identical to that of the solvent in Eq. (2), i.e., $F_0^{\mathrm{A}}[\rho] = F_0^{\mathrm{B}}[\rho] = F_0[\rho]$. The free-energy density due to solvent-particle interactions for component A is also identical to that of the solvent in Eq. (3) and $F_{\mathrm{ps}}^{\mathrm{A}}[\rho] = F_{\mathrm{ps}}[\rho]$. Component A is thus essentially the same as the solvent. Component B, however, differs from the solvent only in the free-energy density of interacting with particles:

$$F_{\mathrm{ps}}^{\mathrm{B}}[\rho^{\mathrm{B}}(\mathbf{x})] = \int \frac{k}{2}\left(\frac{V_{\mathrm{occ}}(\mathbf{x})}{V_{\mathrm{c}}}\right)^2[\rho^{\mathrm{B}}(\mathbf{x})-\rho_{\mathrm{l}}]^2 d^3x. \tag{16}$$

This form of F_{ps}^{B} aims to sink the liquid state of fluid B inside particles. The dynamic evolution of ρ^{A} and ρ^{B} is proposed to follow the advection-diffusion equations with stochastic fluctuations:

$$\frac{\partial \rho^{A}}{\partial t} = -\nabla \cdot \left(\mathbf{J}^{A} + \mathbf{J}_{R}^{A}\right) - \nabla \cdot (\rho^{A}\mathbf{v}), \tag{17}$$

$$\frac{\partial \rho^{B}}{\partial t} = -\nabla \cdot \left(\mathbf{J}^{B} + \mathbf{J}_{R}^{B}\right) - \nabla \cdot (\rho^{B}\mathbf{v}). \tag{18}$$

Here $\mathbf{g}$ is the total momentum density of the fluid mixture and $\mathbf{v} = \mathbf{g}/\rho$ is its velocity field; $\mathbf{J}^{A}$ and $\mathbf{J}^{B}$ are the diffusive mass fluxes and $\mathbf{J}_{R}^{A}$ and $\mathbf{J}_{R}^{B}$ are the corresponding random mass fluxes due to thermal fluctuations. The diffusive mass fluxes are given by $\mathbf{J}^{A} = -\lambda\nabla(\partial F^{A}/\partial\rho^{A})$ and $\mathbf{J}^{B} = -\lambda\nabla(\partial F^{B}/\partial\rho^{B})$. The diffusion coefficients of both fluid components have the same value of λ. The fluctuating fluxes of mass diffusion are modeled as Gaussian white noise with zero mean and covariance determined by the fluctuation-dissipation theorem: $\langle J_{R}^{A^{i}}(\mathbf{x},t)J_{R}^{A^{j}}(\mathbf{x}',t')\rangle = \langle J_{R}^{B^{i}}(\mathbf{x},t)J_{R}^{B^{j}}(\mathbf{x}',t')\rangle = 2\lambda k_{B}T\delta_{ij}\delta(\mathbf{x}-\mathbf{x}')\delta(t-t')$.

Via Eqs. (17) and (18), the fast dynamics of forming fluid-phase boundaries can be controlled by the diffusion and fluctuation fluxes with λ. Provided λ is sufficiently high, liquid B would tightly follow the moving particles while liquid A stays primarily in the bulk, hence realizing the excluded volumes of particles without encountering negative values of ρ. Simulation results indicate that this phenomenology can be achieved by adequately small λ values that are free from causing numerical instabilities in dynamic simulations.

With the dynamics of phase separation decoupled and the vapor phase effectively represented by the space filling of ρ^{B}, the forces caused by free-energy densities would make the solvent density of $\rho = \rho^{A} + \rho^{B}$ fluctuating around the liquid-state value of ρ_{l}. Therefore, the reversible stress tensor in the FHD equations can be modeled as $\mathbf{R} = c_{T}^{2}\nabla\rho$, where c_{T} is the sound velocity at temperature T derived from F_{0} in Eq. (2). This separation of fast dynamics remedies the issue of forming unphysical spurious currents in and out of particles. It is also important to point out that the two fluid components do not interact with each other directly; they are coupled through the interior space of particles.

D. Governing equations of the hybrid FHD and MD methodology

The field variables of the solvent fluid follow the FHD equations that describe the temporal evolution of mass density ρ and momentum density $\mathbf{g}$ [12–16]:

$$\frac{\partial \rho}{\partial t} = -\nabla \cdot \mathbf{g}, \tag{19}$$

$$\frac{\partial \mathbf{g}}{\partial t} = -\nabla \cdot (\mathbf{g}\mathbf{v}) - \nabla \cdot (\mathbf{R} + \mathbf{D} + \mathbf{S}) + \mathbf{f}_{f}. \tag{20}$$

As stated earlier, the fluid velocity is related to the momentum density as $\mathbf{g} = \rho\mathbf{v}$. Here $\mathbf{R}$, $\mathbf{D}$, and $\mathbf{S}$ are the reversible, viscous, and fluctuating stress tensors, respectively, and $\mathbf{f}_{f}$ is the force density that the particle exerts on the fluid.

For the dissipative stress tensor $\mathbf{D}$, we focus on the Newtonian constitutive relation in this work:

$$\mathbf{D} = \eta_{S}(\nabla\mathbf{v} + \nabla\mathbf{v}^{T}) + \left(\eta_{B} - \tfrac{2}{3}\eta_{S}\right)\nabla \cdot \mathbf{v}. \tag{21}$$

The symbols η_{S} and η_{B} are the shear and bulk viscosity, respectively. The conjugate fluctuating stress tensor $\mathbf{S}$ has a Gaussian distribution with respect to ρ whose covariance relates to the dissipation parameters as

$$\langle S^{ij}(\mathbf{x},t)S^{kl}(\mathbf{x}',t')\rangle = 2k_{B}T[\eta_{S}(\delta_{il}\delta_{jk} + \delta_{ik}\delta_{jl}) + \left(\eta_{B} - \tfrac{2}{3}\eta_{S}\right)\delta_{ij}\delta_{kl}]\delta(\mathbf{x}-\mathbf{x}')\delta(t-t'). \tag{22}$$

The superscripts of the matrix components of $\mathbf{S}$ such as S^{ij} enumerate through all three axes of the Cartesian coordinate, i.e., $i,j,k,l = x$, y, or z.

For particulate degrees of freedom in the hybrid model, the dynamics follow Newton's second law

$$M\dot{\mathbf{V}} = \mathbf{F}_{pc} + \mathbf{F}_{ps}, \quad \dot{\mathbf{r}} = \mathbf{V}. \tag{23}$$

For the focused particle with mass M, its velocity and position are $\mathbf{V}$ and $\mathbf{r}$, respectively. The force exerted on the particle by the surrounding solvent fields $\mathbf{F}_{ps}$ is determined from the local force density as

$$\mathbf{F}_{ps} = \int \mathbf{f}_{p}(\mathbf{X})d^{3}\mathbf{X}. \tag{24}$$

Equation (12) is employed to approximate this integral. To comply with the constraint of momentum conservation, our hybrid FHD and MD scheme uses Eq. (10) to adopt

$$\mathbf{f}_{f}(\mathbf{X}) = -\mathbf{f}_{p}(\mathbf{X}). \tag{25}$$

The conservative force on the particle from interactions with other particulate degrees of freedom is $\mathbf{F}_{pc}$. Equation (9) is used to represent $\mathbf{f}_{p}$ with three parts

$$\mathbf{f}_{p}(\mathbf{X}) = -\nabla F_{ps}(\mathbf{X}) - \gamma[\mathbf{V} - \mathbf{v}(\mathbf{X})] + \mathbf{s}(\mathbf{X}). \tag{26}$$

In summary, the equations of motions of our hybrid FHD and MD methodology are Eqs. (20) and (23) coupled with Eqs. (17) and (18). The free-energy densities of Eqs. (1)–(4) are employed with the variation of Eq. (16) for the auxiliary fluid component B. The stress tensors $\mathbf{D}$ and $\mathbf{S}$ are given by Eqs. (21) and (22), respectively. The reversible stress tensor is $c_{T}^{2}\nabla\rho$. The force density of particle-solvent interactions is based on Eqs. (26) and (11) together with Eq. (25).

III. SIMULATION DETAILS

The aforementioned equations are solved by finite differences using cubic Eulerian cells for spatial discretization. In particular, a staggered scheme is employed [12]. This finite difference posits mass densities at cell centers, momentum densities at cell surfaces, and the diagonal and off-diagonal elements of stress tensors at cell centers and corners, respectively. The staggered discretization scheme was shown to allow stable propagation of FHD equations with the sides of each grid cell being as small as 5 Å [12–16].

In this work, water is considered as the default solvent, although the modeling strategy presented above can be applied with different equations of state. The mass density of liquid water is $\rho_{l} = 0.6027$ amu/Å^{3} and the mass density of vapor is set to zero as a practical equivalence. The value of ρ_{v} comes in the hybrid simulation through Eqs. (14) and (15)

to affect the mass fluxes of the two fluids. The values of sound velocity, shear, and bulk viscosity for the liquid water are set to $c_T = 14$ Å/ps, $\eta_S = 19.5$ amu/Å ps, and $\eta_B = 53$ amu/Å ps, respectively. The mass of the solvated particle is $M = \rho_l 4\pi/3R^3$.

The simulations were performed in a cubic box with the side length $a = 210$ Å and at a temperature of 300 K. The simulation box is discretized into $M = 42$ Eulerian cells for each side ($d = a/M$) and $V_c = d^3$. Both the FHD and MD equations are integrated by a second-order Runge-Kutta scheme [34] with the periodic boundary conditions. A time step of 5 fs was found sufficient to provide accurate and stable numerical integration.

In the starting heating period of each simulation, the position of the solute is set randomly at $t = 0$ and the beginning values of the particle and the momentum densities in Eulerian cells are both set to zero. The initial mass densities of the auxiliary fluids are $\rho^A(\mathbf{x}_i) = \rho_l[1 - V_{occ}(\mathbf{x}_i)/V_c]$ and $\rho^B(\mathbf{x}_i) = \rho_l V_{occ}(\mathbf{x}_i)/V_c$. The volume $V_{occ}(\mathbf{x}_i)$ of the ith Eulerian grid occupied by the solute is computed by Eq. (5). After a heating period of 200 ps, the statistical averages are collected every 0.5 ps.

IV. RESULTS AND DISCUSSION

Although the proposed ansatz of hybridizing FHD and MD avoids the unphysical issues of spurious currents and negative densities from occurring in the simulations, the applicability to model nanoscale systems needs to be evaluated by examining if the objectives of capturing the essential equilibrium and nonequilibrium phenomena—solvation free-energy and hydrophobicity, hydrodynamic responses, and thermal equilibrium—could be fulfilled by the hybrid dynamics. In this section, we present the results of applying the hybrid FHD and MD method we developed to an array of case studies to illustrate its general capabilities of achieving these aims.

A. Solvation free energy

The solvation free energy calculated with the FHD and MD method is compared with the all-atom MD result using the extended simple point charge (SPC/E) water model [35]. The solvation free energy of a volume exclusion sphere is proportional to the volume for small sizes and to the surface area for larger ones [31,36,37]. The length scale of transition is 10 Å. As a 5-Å grid is used for both Eulerian and Lagrangian grid cells, the hybrid model can capture this unique behavior of hydrophobicity qualitatively. However, the hybrid model is coarse grained in nature and has limited capability of capturing all of the small-scale behaviors due to a lack of molecular details. Indeed, optimizing the interaction strength k in Eq. (3) to reproduce the all-atom solvation free energies of all solute sizes indicates that the empirical function $k(R) = 2C[\exp(-0.4R) + 0.1]$ fits the data quantitatively. Therefore, as regards the solvation free energy, the effects of missing molecular details can be lumped into this interaction parameter.

The results presented in this section are an average over 100 independent simulations. Each simulation was continued for 1 ns in which the solute was kept fixed at a random position.

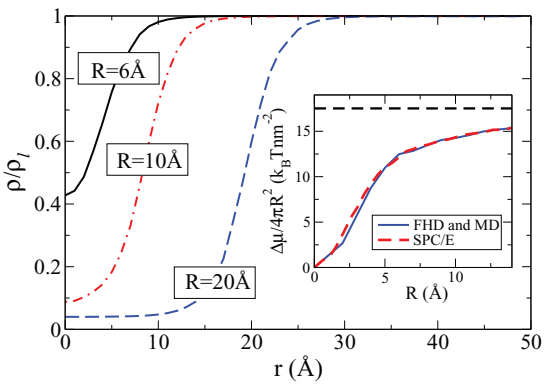

FIG. 2. (Color online) Solvent mass density as a function of the distance from the center of a solute particle for three different sizes $R = 6$, 10, and 20 Å. The inset shows the solvation free energy per k_BT and surface area as a function of the solute size. Squares correspond to the results of hybrid FHD and MD simulations and circles are those from explicit water simulations using the SPC/E model [35]. The dashed line in the inset represents the surface tension energy in the limit of very large solutes.

The profile of fluid mass density around the particle for solutes of three sizes $R = 6$, 10, and 20 Å is shown in Fig. 2. It can be seen that the method of hybridizing particles and fields can resolve the density profile at the solute-solvent interfaces for different particle sizes as the Lum-Chandler-Weeks theory prescribes.

B. Particle dynamics in hybrid FHD and MD simulations

The statistics of translational motions of a solvated particle is examined to illustrate that the thermodynamics and stochastic dynamics due to a fluctuating solvent environment can be captured by the hybrid FHD and MD methodology. The velocity distributions of the solvent and a particle of $R = 20$ Å are shown in Figs. 3(a) and 3(b), respectively. Fitting these profiles to a Maxwell-Boltzmann form gives a very close reproduction of the set temperature of 300 K, $T = 300.2$ K (± 0.5 K) for the solvent and $T = 296$ K (± 3 K) for the particle. Similar accuracy in the statistics of velocity fields was also observed for particles with different sizes in the corresponding FHD and MD simulation. Furthermore, the spatial distribution function of the particle in a Eulerian grid cell is free of bias and local features as shown in Fig. 3(c), indicating that the artifact of finite-size discretization has been eliminated via the scheme described earlier.

For particle diffusion as a result of the white noise in the environment, the Einstein relation defines the diffusion coefficient D as

$$D = \frac{k_B T}{\gamma_{\text{eff}}}, \tag{27}$$

where γ_{eff} is the effective dissipation of the solvent. In general, γ_{eff} is lower than the bare friction γ in Eq. (26) due to the hydrodynamic coupling with the flow profile surrounding the particle that tends to increase the particle mobility. It has been shown that a general expression $1/\gamma_{\text{eff}} = 1/\gamma + 1/\alpha\eta R$, where α is a constant that depends only the lattice geometry and the discretization procedure, can be used to relate γ_{eff}

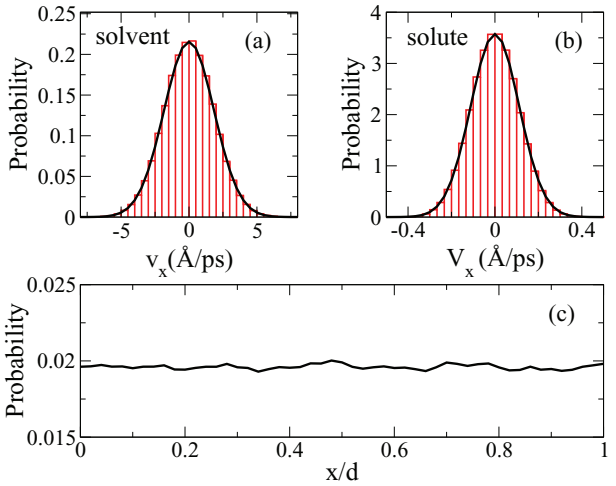

FIG. 3. (Color online) Statistics of particle dynamics in hybrid FHD and MD simulations. The velocity distribution profiles for (a) the solvent and (b) the solute at $T = 300$ K. The solid lines are the best-fit Maxwell-Boltzmann distribution. (c) Spatial distribution of the center of the solute in one of the Eulerian cells of size d. All three distributions are for one of the three Cartesian directions.

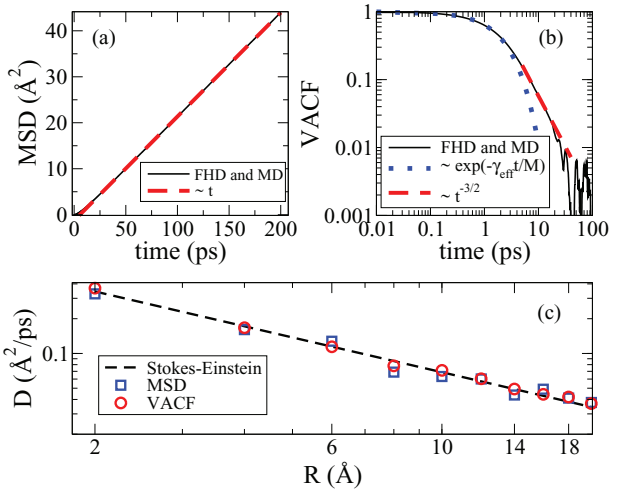

FIG. 4. (Color online) Stokes-Einstein diffusion of a particle simulated via the hybrid FHD and MD methodology. (a) Time dependence of the mean square displacement for a solute of size $R = 20$ Å and at temperature $T = 300$ K. (b) The log-log plot of the normalized velocity autocorrelation function as a function of time for the same solute. The solid line represents the results obtained by the hybrid FHD and MD method. The dotted and dashed lines represent, respectively, the exponential decay at short times and the algebraic relaxation law at long times. (c) The log-log plot of the diffusivity as a function of the solute size. Squares and circles correspond to results obtained from the MSD and VACF, respectively, in comparison with the Stokes-Einstein relation of $D = k_B T/6\pi\eta_S R$ (dashed line).

and γ [17]. Once α is determined for a particular simulation model, one can adjust γ to reproduce the Stokes law, i.e., $\gamma_{\text{eff}} = 6\pi\eta_S R$ [17]. This relation between γ_{eff} and γ was also observed in the results of hybrid FHD and MD simulations and was used to determine γ_{eff} to reproduce stochastic dynamics of solutes in water.

The diffusion coefficient can be calculated from the velocity autocorrelation function (VACF) or the mean square displacement (MSD) as a function of time. Both approaches can be applied with the results of hybrid FHD and MD simulations. The VACF defined as $C(t) = \langle \mathbf{V}(t) \cdot \mathbf{V}(0) \rangle$ drops exponentially at short times, i.e., $C(t) \sim \exp(-\gamma_{\text{eff}} t/M)$, and follows a slower power-law relaxation at long times, i.e., $C(t) \sim t^{-3/2}$ due to hydrodynamic coupling with the surrounding flow profile [7]. The diffusion coefficient can be calculated from the VACF by the Green-Kubo relation

$$D = \frac{1}{3}\int_0^\infty C(t)dt. \tag{28}$$

Alternatively, D can be determined from the slope of MSD with respect to time, $\langle \mathbf{r}^2(t) \rangle = \langle [\mathbf{r}(t) - \mathbf{r}(0)]^2 \rangle$, in the diffusive regime, i.e.,

$$D = \lim_{t\to\infty} \frac{\langle \mathbf{r}^2(t) \rangle}{6t}. \tag{29}$$

In Figs. 4(a) and 4(b) the time dependences of the VACF and MSD, respectively, of a particle of size $R = 20$ Å in a hybrid FHD and MD simulation are presented. It is clear that both functions follow the aforementioned behaviors dictated by the theory, confirming the ability of the hybrid FHD and MD methodology in capturing the hydrodynamic fluctuations in following particle motions at the nanoscale. Similar behaviors were also observed in the simulations of different particle sizes (the results are not shown herein). In Fig. 4(c), the diffusion coefficients computed from Eqs. (28) and (29) for different particle sizes are shown to illustrate the very good reproduction of the Stokes-Einstein relationship of $D = k_B T/6\pi\eta_S R$ via the hybrid FHD and MD simulation method.

C. Collapse of two hydrophobic particles

Hydrophobicity is an important driving force for nanoparticle assembly and dimer aggregation is a classical example to characterize this effect [6,28,38,39]. The ability of incorporating the essential physics: vapor-liquid equilibrium of the solvent, surface tension of the particle-fluid interface, and the Gaussian statistics of density fluctuations in the hybrid FHD and MD method provides an ideal framework to simulate such systems. To illustrate this capability, the collapse of two solutes

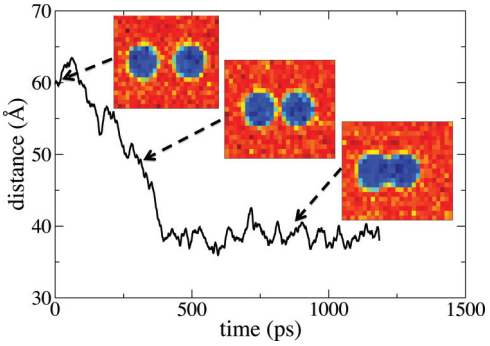

FIG. 5. (Color online) Interpartricle distance of two WCA spheres of $R = 20$ Å as a function of time. The colored density plots represent the mass density of the solvent at three different times. Blue indicates low-mass density and red indicates the value of the liquid-state density.

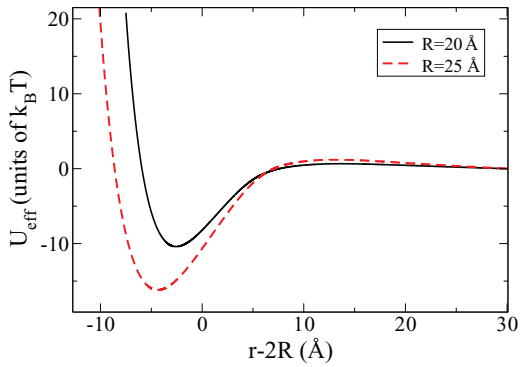

FIG. 6. (Color online) Potential mean force as a function of the distance between two WCA spheres. Solid line corresponds to spheres of $R = 20$ Å and dashed line to spheres of $R = 25$ Å.

interacting via a soft Weeks-Chandler-Andersen (WCA) potential [40]

$$U(r) = \begin{cases} 4\epsilon[(\sigma/r)^1 2 - (\sigma/r)^6] + \epsilon, & r < 2^{1/6}\sigma \\ 0, & r > 2^{1/6}\sigma \end{cases} \quad (30)$$

is simulated with the hybrid FHD and MD method. In Eq. (30), $\sigma = 2R$ and $\epsilon = 1.5k_BT$. To allow the system to relax at any interparticle distance, we extend the simulation box virtually by 10 Å in each direction. At each time step the additional cells are given random mass and momentum densities that satisfy the equilibrium distributions. This way the system is allowed to adjust the excess mass density during the dewetting process.

Figure 5 shows a typical collapsing trajectory via the interparticle distance of two $R = 20$ Å solutes as a function of time. The initial distance between the two particles was 60 Å. In this trajectory, particle aggregation began at 400 ps. After collapse, the two solutes remain bound in the rest of the simulation that was continued for 50 ns. It is clear that the hybrid FHD and MD method can capture the dewetting process encountered during particle aggregation as illustrated in the snapshots of fluid density shown in Fig. 5.

The potential mean force (PMF) for the interparticle separation was also computed to quantify the driving force of hydrophobicity. The force between the two particles is recorded through a stiff harmonic spring of strength c connecting the two particles [41,42]. The equilibrium length L_0 of the spring was set at equally spaced values between $2R - 5$ and $2R + 30$ Å. For each L_0, 100 independent simulations of 2 ns were performed to compute the mean force $F = c(L_0 - \langle r \rangle)$. Shown in Fig. 6 is the PMF for two solutes of size $R = 20$ and 25 Å. As expected, from the result of Fig. 5 we note that the effective free energy has the structure of a strong attractive potential. Note that the minimum of the potential is shifted according to the size of collapsing particles. The depth of the U_{eff} is 10 k_BT for the solute of $R = 20$ Å and $16k_BT$ for $R = 25$ Å.

V. CONCLUSION

Combining mesoscopic solvent modeling with the molecular dynamics of moving particles is an aspired objective of computer simulation. The success of this multiphysics approach in advancing the knowledge of nanoscale self-assembly and dynamics-structure-function relationships of biomolecules, though, relies on the capability of representing the essential forces mediated by the solvent. In this work, we developed an alternative hybrid FHD and MD simulation methodology that can resolve the boundaries between moving particles and solvent fields in Eulerian grid cells. Local free-energy densities of solvent-solute interactions were also devised to realize the excluded volumes of particles. With these functionalities, we showed that both hydrophobicity and hydrodynamics are ubiquitous forces in nature and can be put together in a mesoscopic simulation to capture the phenomena emergent from their coupling. The framework of fluctuating hydrodynamics is chosen for a coarse-grained representation of the solvent and the challenge of mixing Eulerian and Lagrangian variables is thus inevitable in the hybrid FHD and MD methodology. The strategies we devised to overcome the issues of spurious currents, negative densities, and spatially dependent force imbalances—using a pair of auxiliary fluids to realize the excluded volumes of particles and collocating gridding systems to solutes—may also be helpful for similar attempts in other disciplines. The current framework of hybrid FHD and MD simulation also sets the foundation for integrating other important effects mediated by the solvent, such as electrostatics and mass transfer of species concentrations.

ACKNOWLEDGMENTS

We thank the University of California, Berkeley (J.-W.C., N.K.V., and B.Z.S.); Washington State University (N.K.V.); and the National Science Foundation (B.Z.S.) for financial support.

[1] P. Ball, Chem. Rev. **108**, 74 (2008).
[2] J. S. Rowlinson and B. Widom, *Molecular Theory of Capillarity* (Dover, Mineola, NY, 2002).
[3] A. Stannard, J. Phys.: Condens. Matter **23**, 083001 (2011).
[4] F. Bresme and M. Oettel, J. Phys.: Condens. Matter **19**, 3101 (2007).
[5] B. J. Berne, J. D. Weeks, and R. Zhou, Annu. Rev. Phys. Chem. **60**, 85 (2009).
[6] D. Chandler, Nature (London) **437**, 640 (2005).
[7] B. J. Alder and T. E. Wainwright, Phys. Rev. A **1**, 18 (1970).
[8] K. Kadau, T. C. Germann, N. G. Hadjiconstantinou, P. S. Lomdahl, G. Dimonte, B. L. Holian, and B. J. Alder, Proc. Natl. Acad. Sci. USA **101**, 5851 (2004).
[9] T. M. Squires and M. P. Brenner, Phys. Rev. Lett. **85**, 4976 (2000).
[10] J. M. O. de Zárate and J. V. Sengers, *Hydrodynamic Fluctuations in Fluids and Fluid Mixtures* (Elsevier, Amsterdam, 2006).
[11] D. E. Shaw, P. Maragakis, K. Lindorff-Larsen, S. Piana, R. O. Dror, M. P. Eastwood, J. A. Bank, J. M. Jumper, J. K. Salmon, Y. Shan *et al.*, Science **330**, 341 (2010).

[12] N. K. Voulgarakis and J.-W. Chu, J. Chem. Phys. **130**, 134111 (2009).
[13] N. K. Voulgarakis, S. Satish, and J.-W. Chu, J. Chem. Phys. **131**, 234115 (2009).
[14] N. K. Voulgarakis, S. Satish, and J. W. Chu, Mol. Simul. **131**, 552 (2010).
[15] B. Z. Shang, N. K. Voulgarakis, and J.-W. Chu, J. Chem. Phys. **135**, 044111 (2011).
[16] B. Z. Shang, N. K. Voulgarakis, and J.-W. Chu, J. Chem. Phys. **137**, 044117 (2012).
[17] P. Ahlrichs and B. Dünweg, J. Chem. Phys. **111**, 8225 (1999).
[18] G. Giupponi, G. De Fabritiis, and P. V. Coveney, J. Chem. Phys. **126**, 154903 (2007).
[19] M. G. Fyta, S. Melchionna, E. Kaxiras, and S. Succi, Multiscale Model. Sim. **5**, 1156 (2006).
[20] B. Uma, T. N. Swaminathan, R. Radhakrishnan, D. M. Eckmann, and P. S. Ayyaswamy, Phys. Fluids **23**, 73602 (2011).
[21] P. J. Atzberger, P. R. Kramer, and C. S. Peskin, J. Comput. Phys. **224**, 1255 (2007).
[22] M. Uhlmann, J. Comput. Phys. **209**, 448 (2005).
[23] F. B. Usabiaga, I. Pagonabarraga, and R. Delgado-Buscalioni, J. Comput. Phys. **235**, 701 (2013).
[24] F. B. Usabiaga, R. Delgado-Buscalioni, B. E. Griffith, and A. Donev, arXiv:1212.6427.
[25] A. Donev, J. B. Bell, A. L. Garcia, and B. J. Alder, Multiscale Model. Sim. **8**, 871 (2010).
[26] G. De Fabritiis, R. Delgado-Buscalioni, and P. V. Coveney, Phys. Rev. Lett. **97**, 134501 (2006).
[27] A. Dupuis, E. M. Kotsalis, and P. Koumoutsakos, Phys. Rev. E **75**, 046704 (2007).
[28] P. R. ten Wolde and D. Chandler, Proc. Natl. Acad. Sci. USA **99**, 6539 (2002).
[29] S. Popinet and S. Zaleski, Int. J. Numer. Meth. Fluids **30**, 775 (1999).
[30] C. S. Peskin, Acta Numerica **11**, 1 (2002).
[31] K. Lum, D. Chandler, and J. D. Weeks, J. Phys. Chem. B **103**, 4570 (1999).
[32] A. Naji, P. J. Atzberger, and F. L. H. Brown, Phys. Rev. Lett. **102**, 138102 (2009).
[33] S. M. Leitenberger, E. Reister-Gottfried, and U. Seifert, Langmuir **24**, 1254 (2008).
[34] W. Press, S. Teukolsky, W. Vetterling, and B. Flannery, *Numerical Recipes* (Cambridge University Press, New York, 1992).
[35] D. M. Huang, P. L. Geissler, and D. Chandler, J. Phys. Chem. B **105**, 6704 (2001).
[36] P. R. ten Wolde, S. X. Sun, and D. Chandler, Phys. Rev. E **65**, 011201 (2001).
[37] P. Varilly, A. J. Patel, and D. Chandler, J. Chem. Phys. **134**, 074109 (2011).
[38] X. Huang, R. Zhou, and B. J. Berne, J. Phys. Chem. B **109**, 3546 (2005).
[39] X. Huang, C. J. Margulis, and B. J. Berne, Proc. Natl. Acad. Sci. USA **100**, 11953 (2003).
[40] J. D. Weeks, D. Chandler, and H. C. Andersen, J. Chem. Phys. **54**, 5237 (1971).
[41] J. B. Brokaw, K. R. Haas, and J.-W. Chu, J. Chem. Theory Comput. **5**, 2050 (2009).
[42] H. M. Cho, A. S. Gross, and J.-W. Chu, J. Am. Chem. Soc. **133**, 14033 (2011).